ChemPubSoc Europe

DOI: 10.1002/chem.201602681

CHEMISTRY A European Journal Full Paper

Single-Molecule Magnets

Exploring the Slow Relaxation of the Magnetization in Co^{III}-Decorated $\{Dy^{III}_2\}$ Units

Alejandro V. Funes,[a] Luca Carrella,[b] Eva Rentschler,[b] and Pablo Alborés*[a]

Abstract: We have prepared and structurally characterized a new member of the butterfly-like $\{Co^{III}_2Dy^{III}_2\}$ single-molecule magnets (SMMs) through further Co^{III} decoration, with the formula $[Co^{III}_4Dy^{III}_2(OH)_2(teaH)_2(tea)_2(Piv)_6]$ ($teaH_3$ = triethanolamine; Piv = trimethylacetate or pivalate). Direct current (DC) susceptibility and magnetization measurements were performed allowing the extraction of possible crystal-field parameters. A simple electrostatic modeling shows reasonable agreement with experimental data. Alternating current (AC) susceptibility measurements under a zero DC field and under small applied fields were performed at different frequencies (i.e., 10–1500 Hz) and at low temperatures (i.e., 2–10 K). Multiple magnetization relaxation pathways are observed. Comparison with previously reported $\{Co^{III}_2Dy^{III}_2\}$ complex measurements allows an overall discussion about the origin of the dynamic behavior and its relationship with crystal-field split ground multiplet sublevels.

Introduction

Lanthanide ions are at the edge for the development of molecular nanomagnets due to their large single-ion anisotropy. Discrete lanthanide coordination compounds exhibiting well-isolated, magnetically anisotropic ground states can evidence slow relaxation of the magnetization upon application and removal of a magnetic field, that is, bistability behavior.[1] This configures the main characteristic for a single-molecule magnet (SMM). This type of molecules continues to be of great interest due to its unique physical properties like magnetic hysteresis and quantum tunneling of the magnetization (QTM).[2] The main aim behind this research points to potential applications that can exploit these physical properties. The most trailed being: extremely high-density digital information storage devices,[3a–c] quantum information processing,[3a,c–e] and spintronic devices.[4] Since the discovery that single-ion lanthanide complexes can exhibit slow relaxation of the magnetization by showing a larger anisotropic energy barrier (U_{eff}) than the best SMMs transition-metal-based complexes,[5] research into lanthanide nanomagnets has exponentially grown.[1a,c,6] The magnitude of such barrier is a fundamental feature, often considered as a measure of quality of a SMM as it rules the stability of the orientation of the magnetization upon application and removal of a magnetic field at a given fixed temperature. In fact, the larger the energy barrier, the longer the relaxation time at a fixed temperature, under the critical condition that quantum tunneling relaxation mechanism (QTM) can be successfully suppressed. Following this mainstream several mono- and polynuclear lanthanide[1a,d,7] and polynuclear heterometallic 3d–4f coordination complexes[8] have been prepared with the aim of getting improved properties, namely longer relaxation times (higher U_{eff}) at higher temperatures and with mitigated QTM.[6] Several reviews have discussed the background about the observation of SMM behavior in a single-lanthanide compound.[1a–c,8c] The main aspect points to the ligand field around the Ln^{III} ion, which fine tunes the *mJ* magnetic microstates energy by splitting of the *J* ground multiplet. The energy difference from the ground state to the first excited state often correlates to the magnitude of the barrier height. As a direct consequence, any subtle change in the geometry and ligand environment around the Ln^{III} site can drastically modify these sub-level splittings and hence the dynamic of the magnetization relaxation.

In this context, a series of butterfly-like $\{Co^{III}_2Dy^{III}_2\}$ SMMs have been reported during the last years,[9] including our own contribution, $[Co^{III}_2Ln^{III}_2(OCH_3)_2(teaH)_2(Piv)_6]$ ($teaH_3$ = triethanolamine; Piv = trimethylacetate or pivalate), which is up to now, the only example within this series that show two resolved relaxation pathways under a zero DC external applied field.[10] A second example with two well resolved relaxation processes based on the acac ligand, $[Dy^{III}_2Co^{III}_2(OH)_2(teaH)_2(acac)_6]$ (acac = acetylacetonate) has recently been reported, but with two independent molecules in the unit cell. All along this family of complexes, it is observed that very subtle changes in the coordination spheres of the metallic centers provoke dras-

[a] A. V. Funes, Prof. Dr. P. Alborés
Departamento de Química Inorgánica, Analítica y Química Física/ INQUIMAE (CONICET), Facultad de Ciencias Exactas y Naturales
Universidad de Buenos Aires, Pabellón 2, Ciudad Universitaria
C1428EHA Buenos Aires (Argentina)
E-mail: albores@qi.fcen.uba.ar

[b] Dr. L. Carrella, Prof. Dr. E. Rentschler
Institute of Inorganic and Analytical Chemistry
Johannes Gutenberg University of Mainz
Duesbergweg 10–14, 55128 Mainz (Germany)

Supporting information for this article can be found under http://dx.doi.org/10.1002/chem.201602681.

tic changes in the magnetic behavior, namely the magnetization relaxation processes.

We are now reporting a new member of this family, that is, $[Co^{III}_4Dy^{III}_2(OH)_2(teaH)_2(tea)_2(Piv)_6]$ (**1**), where the local environment of the Dy^{III} is affected through remote decoration of the butterfly $\{Co^{III}_2Dy^{III}_2\}$ core with additional close-shell Co^{III} ions. We are presenting a detailed magnetic study focused on the dynamic properties and making the comparison of this new $\{Co^{III}_4Dy^{III}_2\}$ core with the closely related $[Co^{III}_2Ln^{III}_2(OCH_3)_2(teaH)_2(Piv)_6]$ (**2**) previously reported.[10]

Results and Discussion

Synthesis and structural characterization

In the last time we have been exploiting the versatility of the complex $[Co_2(\mu\text{-}H_2O)(Piv)_4(HPiv)_4]$ as a precursor for building up molecular clusters including Co^{II} and/or Co^{III} ions.[11] We have explored its reaction with lanthanide sources, in particular with nitrate hydrates, $Ln(NO_3)_3{\cdot}xH_2O$, in the presence of the versatile triethanolamine ($teaH_3$) ligand. Reactions performed in acetonitrile with the addition of triethylamine as a base for deprotonation of the $teaH_3$ ligand, affords the compound $[Co^{III}_2Dy^{III}_2(OCH_3)_2(teaH)_2(Piv)_6]$. This compound appears particularly interesting regarding its magnetization relaxation dynamic properties.[10] Hence, we decided to further explore the reaction of $[Co_2(\mu\text{-}H_2O)(Piv)_4(HPiv)_4]$ with Dy^{III} nitrate in the presence of the $teaH_3$ ligand. We found that employing methanol as solvent and keeping triethylamine as base affords a new $\{Dy^{III}_2\}$-based complex with a higher content of Co^{III} ions in comparison with the previously reported complex $[Co^{III}_2Dy^{III}_2(OCH_3)_2(teaH)_2(Piv)_6]$, with the formula $[Co^{III}_4Dy^{III}_2(OH)_2(teaH)_2(tea)_2(Piv)_6]$. The inclusion of two $[Co^{III}tea]$ moieties in this new complex **1**, provokes changes in the coordination sphere of the Dy^{III} as will be discussed hereafter.

The asymmetric unit of the monoclinic C_{2c} cell consist of half of the molecule due to the presence of a C_2 rotation axis, which makes both coordination spheres of the Dy^{III} crystallographically equivalent (Figure 1). The metal core displays a *syn–syn* butterfly-like arrangement in contrast to compound **2**, $[Co^{III}_2Dy^{III}_2]$, where the arrangement is a *syn–anti* one.[10]

The additional Co^{III} sites appear fused through a μ_3-alkoxide bridge to both sides of the butterfly structure (Figure 2). As in complex **2**, the outer "wing" positions are occupied by Co^{III} ions whereas the Dy^{III} ions are placed at the body sites. Each Dy^{III} ion is coordinated with two μ_3-hydroxide ligands (two μ_3-methoxide ligands are present in complex **2**), two μ_2-O atoms of the opposing doubly and fully deprotonated $teaH_3$ ligands (both doubly deprotonated in the case of complex **2**), two μ_2-O atoms of adjacent pivalate ligands (opposing pivalate ligands in case of complex **2**), and finally by an O atom of a κ^1-pivalate ligand and a μ_3-O atom of a doubly deprotonated $teaH_3$ ligand (both O atoms of a κ^2-pivalate ligand in the case of complex **2**). The crystallographically unique Dy^{III} ion is eight-coordinate with a distorted SAP (square-antiprism) geometry and Ln–O bond lengths in the range of 2.270(6)–2.571(5) Å. Analysis of the coordination geometry of the Dy^{III}, with

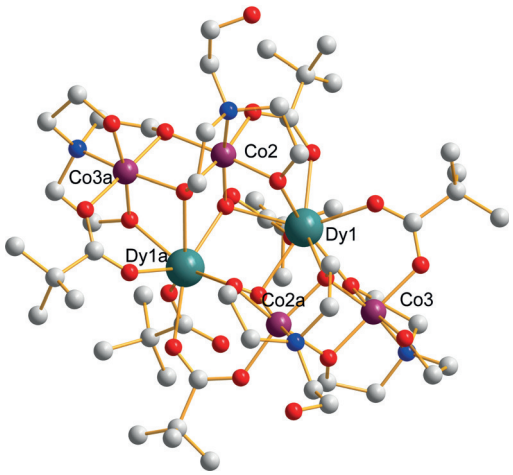

Figure 1. Molecular representation of the crystal structure of complex **1**. Hydrogen atoms are omitted for clarity. Symmetry operations: a) $2-x, y, 3/2-z$.

SHAPE,[12] shows a minimum continuous shape measure (CShMs) for a SAP geometry with a value of 0.793. Values of the CShM between 0.1 and 3 usually correspond to a not negligible but still small distortion from ideal geometry. The present CShM value clearly contrasts with that observed for the environment of the Dy^{III} in complex **2**, that is, 1.889. When looking closer to the Dy–O bond lengths a clear pattern is found: one short bond length, that is, 2.270(6) Å ($Dy-\mu_2O_{alkoxide}$), one long bond length, that is, 2.571(5) Å ($Dy-\mu_3O_{alkoxide}$), and six intermediate bond lengths spanning a range of 2.320(5)–2.397(5) Å. Long and short bond lengths correspond to adjacent Dy–O bonds. For complex **2** the following pattern is found: two short bond lengths, that is, 2.253(3) and 2.261(4) Å (both $Dy-\mu_2O_{alkoxide}$), three long bond lengths spanning a range of 2.446(4)–2.455(5) Å, (two $Dy-\mu_2O_{hydroxides}$ and a $Dy-O_{pivalate}$), and three intermediate bond lengths spanning a range of 2.360(3)–2.389(4) Å. Both short bond lengths correspond to almost opposing Dy–O bonds (angle of 143.2(1)°). Both independent Co^{III} ion sites are in a six-coordinated, octahedral environment, with Co–O bond lengths in the range of 1.888(5)–1.972(5) Å and a Co–N bond length in the rang 1.915(7)–2.001(6) Å, characteristics of a Co^{III} oxidation state. The four Co^{III} sites are arranged in two dimeric units held by double μ_2-alkoxide bridges.

Intramolecular hydrogen-bond interactions are observed between the μ_2-hydroxido ligands and the non-coordinating O atoms of the κ^1-pivalate ligands. The free pivalic acid is kept at short distance from complex **1** through hydrogen-bond interactions with the fully deprotonated coordinated $teaH_3$ ligand (see the Supporting Information).

No strong intermolecular interactions are observed in the crystal packing of complex **1** in contrast with complex **2** where hydrogen-bond interactions held the molecules in chains.[10] In this case, solvent methanol molecules mediate, through multiple hydrogen-bond interactions, the main intermolecular contacts running along the monoclinic *b* direction (see the Supporting Information). The intermolecular closest Dy···Dy distance is 12.187(2) Å, which is more than three times larger

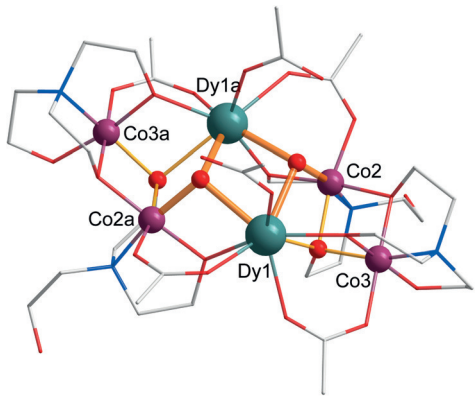

Figure 2. Molecular representation as balls and sticks model complex **1**, highlighting the metals butterfly-like core arrangement of the complex. Hydrogen atoms and *tert*-butyl groups are omitted for clarity. Symmetry operations: a) $2-x, y, 3/2-z$.

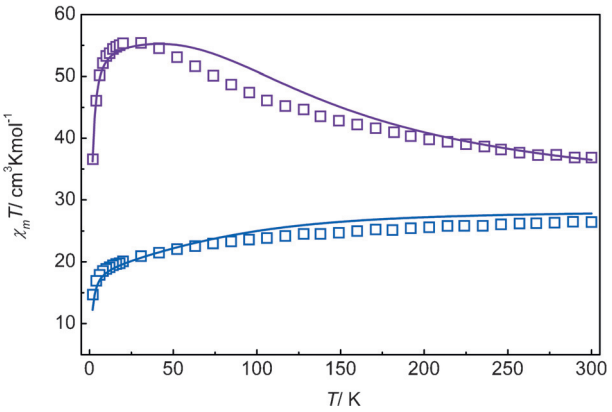

Figure 3. $\chi_m T$ versus T data plots of complex **1** (open squares) at 1 kOe between 2–300 K. The full line shows the simulated data with parameters described in the text.

than the intramolecular Dy–Dy bond length of 3.7764(9) Å. This larger intermolecular Dy···Dy distance in comparison with that observed in complex **2** (8.301 Å) cannot be attributed to the absence of direct hydrogen-bond interactions; as also in the case of compound **2**, the closest Dy···Dy distance is not along the hydrogen-bond network propagation. Instead, the presence of methanol solvent molecules, as well as free pivalic acid molecules, is probably the promoter of the larger spacing between molecules of complex **1** in comparison with that observed in the crystal packing of complex **2**.

DC magnetic properties

Direct current (DC) magnetic susceptibility measurements were performed on single crystals crop of the reported complex in the temperature range 2–300 K and in an applied field of 1 kOe under two different conditions, that is, without preventing free movement of the crystallites under the applied magnetic field and preventing it by silicone grease embedding (Figure 3). The room-temperature $\chi_m T$ value of the fixed sample, 26.5 cm^3 mol^{-1} K, is relatively close to the expected value for two non-interacting Dy^{III}, that is, 28.3 cm^3 mol^{-1} K, under spherical symmetry. Upon cooling, the $\chi_m T$ values falls gradually down to 30 K where it plummets to reach a value of 14.7 cm^3 mol^{-1} K at 2 K. This behavior is attributed to the depopulation of the crystal field split *mJ* sublevels, with also a possible onset of weak antiferromagnetic exchange and/or dipolar interactions between both Dy^{III} sites, mainly contributing at very low *T*. The $\chi_m T$ versus *T* data profile of the non-restrained sample appears clearly different when compared to the restrained sample data. The room-temperature $\chi_m T$ value is clearly above the value observed for the restrained sample suggesting field alignment of the crystallites due to magnetic moment torquing. A continuous increase of the $\chi_m T$ values upon cooling is observed up to 26 K, where a sharp decrease is finally achieved. This behavior supports the idea of crystallites field alignment and also suggests a crystal field mainly stabilizing higher values of *mJ*. We have already observed this behavior for the previously reported magnetic data of compound **2**.[10]

The *M* versus *H* isotherm plot at low temperature, that is, in the range of 2–10 K, shows a rapid increase in *M* below 10 kOe, before saturating at a value of 9.4 Nβ in the case of the restrained sample (Figure 4). The expected magnetization saturation value for two isolated Dy^{III} ions is ($2g_J J$) 20 Nβ, which is clearly above the experimentally observed value, evidencing a strong crystal field splitting of the different *mJ* components of the ground *J* state.

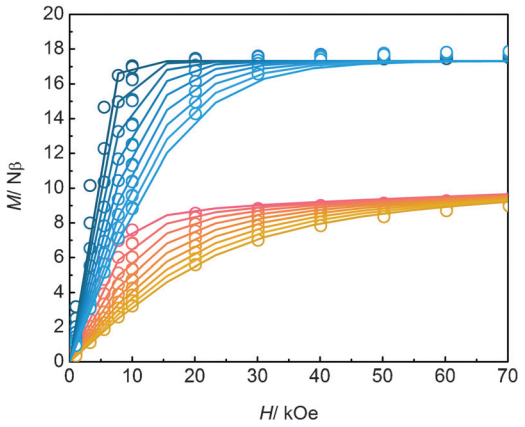

Figure 4. M versus H data plots (open symbols) between 2–10 K (light to dark) in the range of 1–70 kOe for complex **1**. The full line shows the simulated data with parameters described in the text. Red palette = silicone embedded sample, blue palette = free sample.

On the other hand for the unrestrained sample a saturation value of 17.8 Nβ is observed. The abrupt saturation in this case, when comparing with the profile of the restrained sample, becomes an additional support of the field-induced orientation of the crystallites (Figure 4). The expected *M* saturation value for a completely aligned sample of a Dy^{III} ion along the main quantization axis must equal $g_J m_J$ for an isolated ground *mJ* doublet state. In the previous studies of compound

2, a saturation value of 20 Nβ was observed,[10] which is in agreement with the expected saturation value for a completely oriented sample along the main quantization axis for $mJ=\pm 15/2$ with $g_J=4/3$. This was a definitive evidence of an $mJ=\pm 15/2$ ground state doublet. In the case of compound **1**, two different situations can be envisioned, that is, an $mJ=\pm 13/2$ ground doublet state, where for a completely aligned sample a magnetization saturation value of 17.3 Nβ (for two Dy^{III} sites) is expected or an $mJ=\pm 15/2$ ground doublet state with possibly a very small admixture of low-lying excited states due to non-axial crystal-field components. In the case of compound **2**, we have previously shown that it is possible to simultaneously account for all the DC magnetic data (restrained and not restrained samples) behavior through employment of a Hamiltonian for two isolated and equivalent magnetic moments $J=15/2$ (Dy^{III} ion; ${}^6H_{15/2}$, $S=5/2$, $L=5$, $J=15/2$, $g_J=4/3$) and a crystal-field term expressed as Stevens equivalent operators[10] [Eq. (1)]:

$$\hat{H} = g_J\beta H(\hat{J}_1+\hat{J}_2)+\sum_{k=2,4,6}\sum_{q=-k\ldots k} B_q^k(\hat{O}_{1q}^k+\hat{O}_{2q}^k) \quad (1)$$

We hence followed the same procedure for complex **1**. Fitting the data by using the PHI package,[13] which affords a reasonable agreement with the experimental data employing in this case four CF parameters of all possible allowed for a SAP (D_4d) geometry: $B_2^0=(-1.0\pm 0.5)$, $B_4^0=(5\pm 4)\times 10^{-4}$, $B_6^0=(1\pm 2)\times 10^{-4}$, and $B_4^4=(1\pm 1)\times 10^{-2}$ cm^{-1}. It is clear that this is a minimum satisfactory set of crystal-field terms, but not a complete one, as far as the Ln^{III} site is not under an ideal D_4d symmetry. In the case of the DC magnetic data of compound **2**, a simultaneous agreement was achieved with only two CF parameters,[10] namely $B_2^0=(-2.4\pm 0.2)$ and $B_4^0=(3\pm 2)\times 10^{-3}$ cm^{-1}, affording a ground doublet state with maximum $mJ=\pm 15/2$. In order to avoid over-parameterization, crystal-field terms had been added one-by-one after checking that no reasonable simultaneous fitting was possible before the addition of the next parameter. In order to improve the lowest $\chi_m T$ temperature data a HDVV exchange interaction term (which operates only over the spin component of states) between both Dy^{III} ions was added [Eq. (2)]:

$$\hat{H} = g_J\beta H(\hat{J}_1+\hat{J}_2)+\sum_{k=2,4,6}\sum_{q=-k\ldots k} B_q^k(\hat{O}_{1q}^k+\hat{O}_{2q}^k)-2J_{exc}\hat{S}_1\hat{S}_2 \quad (2)$$

From a fitting with the optimized crystal-field parameters fixed, $J_{exc}=(-0.05\pm 0.02)$ cm^{-1} is obtained, which is very similar to the one found for compound **2**. Most of the reported $\{Dy_2-\mu O_2\}$ systems where an exchange (or dipolar) interaction is discussed, are based on theoretical calculations,[9a,c,f,14] with a recent notable example of a direct experimental determination of Dy–Dy interaction.[14b] In all cases the observed magnitude of the exchange interaction is in the same order of magnitude as the one found for compounds **1** and **2**.

The CF parameters obtained, reflect the existence of a non-axial contribution, in this case through the B_4^4 parameter, but this is at some point arbitrary as another non-axial contribution could probably be employed. The obtained ground doublet state is described essentially as $mJ=\pm 13/2$ (99%) with an effective g value of 17.3, which is in agreement with the observed magnetization saturation value. The first excited doublet state is $mJ=\pm 11/2$ at an energy of 150 cm^{-1} followed by $mJ=\pm 1/2$ at 194 cm^{-1} (see the Supporting Information).

At this point, nothing can be said about the main quantization axis orientation relative to the Dy^{III} ligand environment coordinates. In the case of complex **2**, where the ground doublet state is undoubtedly $mJ=\pm 15/2$, the MAGELLAN package[15] can be employed to obtain information about the relative orientation of the magnetic moment. This approach relies on a pure point charge (n charges of q_n charge) electrostatic crystal field arising from the crystal structure coordinates (θ_n, ϕ_n) [Eq. (3)]:

$$V_{CF}(\theta,\varphi)=\sum_{k=2,4,6}\sum_{q=-k\ldots k}\sum_n \frac{4\pi}{2k+1}(-1)^q\frac{q_n\langle r^k\rangle Y_k^q(\theta,\varphi)Y_k^q(\theta_n,\varphi_n)}{R_n^{k+1}} \quad (3)$$

The minimization of the electrostatic energy due to the crystal field (V_{CF}) for the ground $mJ=\pm 15/2$ doublet state (expanded in terms of Y_2^0, Y_4^0, and Y_6^0) with respect to the relative orientation of the main quantization axis (θ, ϕ) affords the final predicted axis.

In the case of compound **2**, it is found that this axis runs close to the two short Dy–O bonds (see the structural discussion), almost orthogonal to the expected main axis of the SAP arrangement. This result shed light on the real crystal-field environment that now shows to be much closer to a BTPR (biaugmented trigonal prism; C_2v), than to the SAP (D_4d) determined from mere crystal coordinate evaluation. In fact, the BTPR geometry is the second one with lowest CShM from the SHAPE algorithm (2.249). The main axis runs close to the pseudo C_3 axis of the triangular prism but orthogonal to the C_2 axis of the BTPR symmetry (Figure 5). This becomes a quite important result showing that pure geometrical considerations are not enough to define the CF environment.

In the case of compound **1**, the lack of a $mJ=\pm 15/2$ doublet ground state precludes the employment of the MAGELLAN package approach. However, a more general method can be attempted once a set of experimentally determined CF parameters has been obtained. It is possible from a pure point charge model (as well as MAGELLAN) to obtain calculated CF parameters for all possible orientations of the main quantization axis. Then it is sufficient to search for those orientations that match the calculated CF parameters with the experimental ones.

As already shown by other authors in similar approaches,[16] the CF parameters B_k^q can be evaluated from Equations (4) and (5):

$$A_k^q=\frac{4\pi}{2k+1}c_{kq}(-1)^q\sum_{i=1..N}\frac{|q_i|\langle r^k\rangle Y_k^{-q}(\theta_i,\varphi_i)}{R_i^{k+1}} \quad (4)$$

$$B_q^k=A_q^k\langle r^k\rangle\alpha^k \quad (5)$$

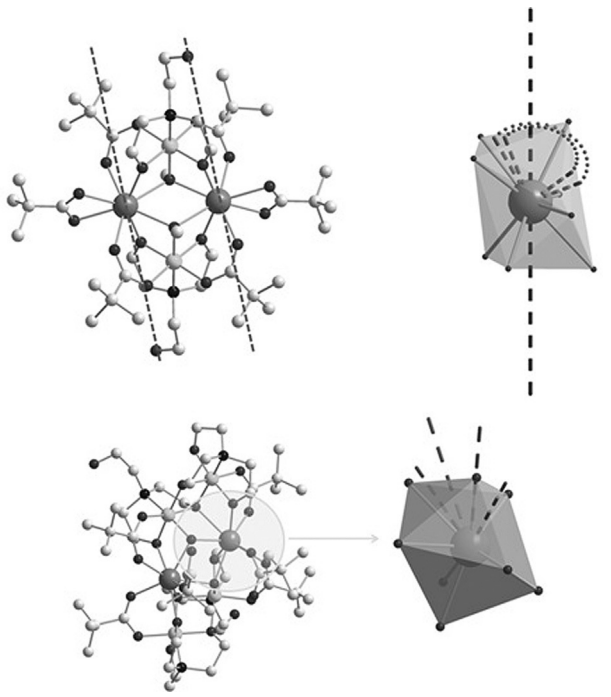

Figure 5. Main orientation of the quantization axis of the magnetic moment of Dy^{III}. Top: compound **2** as arising from the MAGELLAN package (left) and its comparison with the CF-based calculation (right, dotted lines). Bottom: compound **1**, CF-based calculated possible orientations.

where α^k are the Stevens operators equivalence factors, $<r^k>$ are the radial integrals, and c_{kq} are the conversion factors from spherical harmonics to the Stevens operators.

In order to test this approach and employing the same charge point modeling as MAGELLAN, we performed the hemisphere exploration of all B_k^q CF parameters for the Dy^{III} environment of complex **2**. Then, we searched for those orientations that afford values of B_2^0 and B_4^0 close to the experimental ones. The obtained orientations of the main axis showed a good agreement with the MAGELLAN results (Figure 5). In the case of complex **2**, a range of possible orientations is obtained due to the existence of only two experimental established CF parameters (the span CF values are $B_2^0 = -2.3 - -1.9$ and $B_4^0 < 5 \times 10^{-3}$ cm^{-1}).

The same procedure was applied for complex **1**, where four experimental CF parameters are available. As expected, in this case a smaller number of main axis directions is obtained (Figure 5). Two different BTPR arrangements are implied where the main axis lies close to the short Dy–O bond or to the long Dy–O bond (see the structural discussion). Both directions correspond again to the pseudo C_3 axis of the triangular prism. It is clear, as in the case of complex **2**, that the pure geometrical SAP description is not reflecting the real CF environment. Here, again from the SHAPE algorithm the next smallest CShM points to a BTPR symmetry (1.590).

It seems that the main quantization axis of complex **2** fits better to the BTPR description than for complex **1**, due to the presence of two opposite short Dy–O bonds. This could explain the presence of non-negligible non-axial CF parameters in the latter case.

It is worth notifying that this simplified point charge model can, at best, offer a semi-quantitative picture of the crystal field manifold splitting of the electronic ground term of the Dy^{III}.

Dynamic magnetic properties

For compound **2**, we have previously studied a possible slow relaxation of magnetization mechanisms at low temperature.[10] Alternating current (AC) magnetic susceptibility measurements show a temperature and frequency dependence of the out-of phase (χ_m'') components of the susceptibility in a zero DC field. Noticeably and differing from the behavior observed in all the other reported $\{Co^{III}_2Dy^{III}_2\}$ systems,[9] two well-resolved peak maxima in χ_m'' were observed up to 9.5 K, with Cole–Cole plots constructed between 2.5–9.5 K, revealing two convoluted semicircular plots and reflecting two single relaxation mechanisms with clearly differing timescales. These dynamic data can be well reproduced considering a combination of an Orbach with a quantum tunneling mechanism for the slower process and a combination of an Orbach and Raman mechanism for the faster relaxation process. We have shown that the obtained values for the thermal barriers describing the Orbach pathways compare quite well with the low-lying energy multiplets arising from the crystal-field splitting parameters experimentally extracted from the DC magnetic data.[10] The related compound **1**, also show a temperature and frequency dependence of the out-of-phase (χ_m'') component of the susceptibility in a zero DC field; but only one relaxation process can be distinguished up to 10 K (Figure 6).

The increasing of a tail in the low-temperature range suggests an onset of a second relaxation process. Fitting of Cole–Cole plots through a generalized Debye model [Eq. (6)] allowed the extraction of relaxation times within a temperature range of 2–8.5 K with α values spanning 0.19–0.32 (Figure 6).

$$\chi_{ac} = \chi_S + \frac{\chi_T - \chi_S}{1 + (i\omega\tau)^{(1-\alpha)}} \quad (6)$$

The temperature dependence of these characteristic relaxation times can be further analyzed in terms of the following general Equation (7).[17]

$$\frac{1}{\tau} = C_{Direct}T + C_{Ram}T^n + \frac{1}{\tau_{QT}} + \frac{1}{\tau_0}exp\left(-\frac{U_{eff}}{T}\right) \quad (7)$$

Here, the exponential term corresponds to the Orbach mechanism, distinctive due to its thermal barrier parameter and recognized through a linear $\ln\tau$ versus T^{-1} plot. When looking at the $\ln\tau$ versus T^{-1} plot (Figure 6), a linear regime at high temperatures reaching an also clear plateau at lower temperatures is readily identified. These observations suggest that an Orbach mechanism is operative with an onset of a quantum tunneling relaxation mechanism, as already suggested from the out-of-phase susceptibility profile. However, as commonly observed in Ln^{III}-based systems, it is not possible to fit the whole temperature data range employing only these two re-

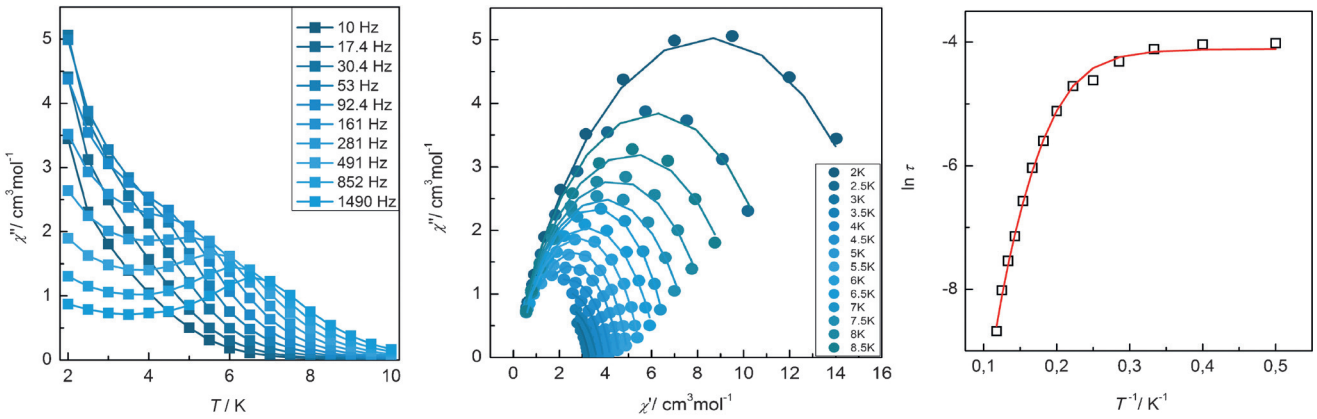

Figure 6. Left: frequency dependence of the out of-phase AC susceptibility χ_m'' of compound **1** in a zero DC magnetic field in the temperature range 2–10 K. Middle: Cole–Cole plots (circles) with best fitting (see text; lines) in the temperature range 2–8.5 K. Right: $\ln\tau$ versus T^{-1} plots (open symbols) together with best fitting plots (see text; full line). Time is given in seconds.

laxation mechanism. It is necessary to add a Raman term [i.e., the second one in Eq. (7)].

Two, in quality almost identical, best fitting parameter sets are obtained with $n=5$ or 7, that is, $U_{eff}=78$ K, $\tau_0=2.9\times10^{-8}$ s, $C_{Ram}=3.6\times10^{-2}$ s^{-1} K^{-5}, and $\tau_{QT}=1.8\times10^{-2}$ s ($n=5$) and $U_{eff}=115$ K, $\tau_0=1.2\times10^{-9}$ s, $C_{Ram}=1.3\times10^{-3}$ s^{-1} K^{-7}, and $\tau_{QT}=1.6\times10^{-2}$ s ($n=7$). It can be seen that there is a strong correlation between the Orbach and Raman parameters leaving an uncertainty in the thermal barrier value, which could be found in the range spanned by both obtained values. These dynamic parameter values are similar to the observed one for the fast process in compound **2**, where it was also necessary to include a Raman term in addition to the thermal-activated Orbach mechanism.[10] From the DC magnetic data fitted CF parameters of complex **1**, the estimated energy difference between the ground doublet state ($mJ=\pm13/2$) and the first excited doublet state ($mJ=\pm11/2$) is about 150 cm^{-1}. This appears larger but still in the magnitude order than the obtained thermal barrier from the dynamic experimental data.

In order to get more insight into the magnetization relaxation dynamic in these Co^{III}-decorated {Dy$^{III}_2$} systems, we explored the AC susceptibility data dependence under an external applied small DC field for both complexes **1** and **2**. We performed an external static field scanning of the AC out-of phase susceptibility response at 2 K spanning a range of 0–3 kOe at driving frequencies between 10–1500 Hz (see the Supporting Information).

For complex **2**, a frequency-independent profile with a maximum at approximately 1500 Oe is observed. The overall magnitude of the out-of-phase response decreases with an increasing frequency. A more complex profile is observed for the data of complex **1**, where two maxima can be clearly distinguished at 500 and 2500 Oe. On increasing the frequency, the maximum positions smoothly shift to 1200 and 1600 Oe, with a diminishing of the out-of-phase response.

To further analyze the field dependence of the AC data, we performed a complete frequency- and temperature-dependence measurement at selected external DC fields. We chose those fields where a maximum or a minimum was observed in the χ'' versus H data profile, that is, 500, 1500, and 2200 Oe (for compound **1**) and 1500 Oe (for compound **2**).

Regarding complex **2**, the temperature- and frequency-dependent profiles of χ'' preserve the same main features observed under an applied external zero field. Two relaxation processes can be observed but with lower resolution (Figure 7). In the χ'' versus T data plot, and at higher frequencies, a tailing at low temperatures becomes noticeable, suggesting an onset of a third relaxation process. This had not been observed in the zero DC data.[10] The Cole–Cole plots clearly evidences these three relaxation processes, which can be identified when sweeping the temperature (Figure 7).

Through the generalized Debye expression given in Equation (6) or the corresponding for two overlapped processes [Eq. (8)] it was possible to extract the relaxation characteristic times in the temperature range 2.5–10 K with α values spanning a broad range of 0.0–0.62.

$$\chi_{AC}(\omega)=\chi_{S,tot}+\frac{\Delta\chi_1}{1+(i\omega\tau_1)^{(1-\alpha_1)}}+\frac{\Delta\chi_2}{1+(i\omega\tau_2)^{(1-\alpha_2)}} \quad (8)$$
$$\chi_{S,tot}=\chi_{S1}+\chi_{S2} \qquad \Delta\chi_{1,2}=\chi_{T1,2}-\chi_{S1,2}$$

The temperature dependence of these characteristic relaxation times shows a behavior similar to the one observed under a zero DC field but with an additional process, mainly temperature independent, at low temperature (from 2.5 to 4 K; Figure 7). We employed Equation (7) to fit the $\ln\tau$ versus T^{-1} data plots. For the slow relaxation process (S), two best fitting parameter sets that are almost identical in quality are obtained with $n=5$ or 7, that is, $U_{eff}=89$ K, $\tau_0=5.4\times10^{-8}$ s, $C_{Ram}=5.5\times10^{-3}$ s^{-1} K^{-5} ($n=5$) and $U_{eff}=104$ K, $\tau_0=2.2\times10^{-8}$ s, $C_{Ram}=1.7\times10^{-4}$ s^{-1} K^{-7} ($n=7$). Notably, a reasonable fit including only the Raman component of Equation (7) with $n=7$ and $C_{Ram}=2.2\times10^{-4}$ s^{-1} K^{-7} ($n=7$) can be obtained. This result shows that the existence of the thermal-activated Orbach contribution cannot be univocally established. In the case of the fast relaxation process (F) an excellent fit is obtained with the following parameters: $U_{eff}=59$ K, $\tau_0=1.7\times10^{-7}$ s, and $\tau_{QT}=0.58$ s. In this case

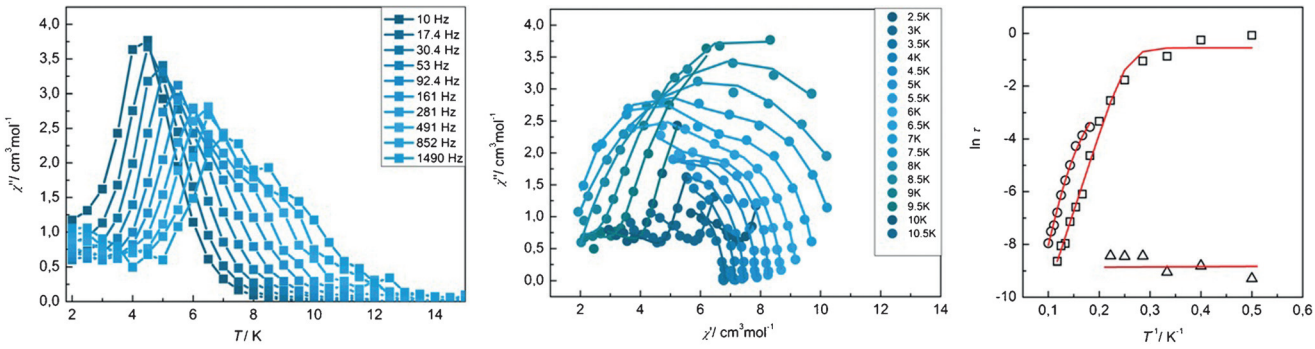

Figure 7. Left: frequency dependence of the out-of-phase AC susceptibility χ_m'' of complex **2** at a 1500 Oe DC magnetic field in the temperature range 2–10 K. Middle: Cole–Cole plots (circles) with best fitting (see text; lines) in the temperature range 2–8.5 K. Right: $\ln\tau$ versus T^{-1} plots (open symbols) together with best fitting plots (see text; full line). Circles = slow process (S), squares = fast process (F), triangles = temperature-independent process. Time is given in seconds.

a linear Arrhenius regime without Raman contribution is clearly observable. Finally, the temperature-independent relaxation process observed, which must be attributed to magnetization quantum tunneling, exhibits a characteristic time $\tau_{QT} = 2.0 \times 10^{-4}$ s.

Dynamic parameters obtained for the slow (S) and fast (F) processes in complex **2**, compare well with the ones observed under an applied zero DC field. Surprisingly, the quantum tunneling characteristic time of the F process is one order of magnitude smaller than under a zero DC field. It is normally assumed that the application of a small static field suppresses QT pathways. However, in the case of slightly exchange or dipolar coupled Dy^{III} ions this conclusion is not straightforward.

From the out-of-phase susceptibility response field scanning at 2 K it is possible to extract the characteristic relaxation times at each different static DC field from Cole–Cole plot fittings in a similar manner as with the temperature AC data scanning. As two distinct relaxation processes with clear different characteristic times can be distinguished (see the Supporting Information and Figure 8), Equation (8) was employed.

The field dependence of the relaxation times can then be evaluated through Equation (9) suitable for a Kramer ion:

$$\frac{1}{\tau} = A_1 H^4 T + \frac{B_1}{1 + B_2 H^2} \qquad (9)$$

where the first term corresponds to the direct relaxation process whereas the second one is related to the temperature-independent quantum tunneling relaxation process.[17] In the case of the fast process a reasonable fitting can be obtained with the following parameters: $A_1 = 1.0 \times 10^{-9}$ s^{-1} K^{-1} Oe^{-4}, $B_1 = 844$ s^{-1} and $B_2 = 1.4 \times 10^{-6}$ Oe^{-2}. It can be seen that the relaxation time diminishes two orders of magnitudes up to 1 kOe due to the dominant direct mechanism. When looking at the slow process a more complex picture is observed, where two overlapping relaxation pathways are distinguished. It is possible to account for them through Equation (9) for each independent pathway: $A_1 = 5.2 \times 10^{-13}$ s^{-1} K^{-1} Oe^{-4}, $B_1 = 135$ s^{-1}, and $B_2 = 3.5 \times 10^{-4}$ Oe^{-2} for the slower process and $A_1 = 6.0 \times 10^{-15}$ s^{-1} K^{-1} Oe^{-4}, $B_1 = 5.1$ s^{-1}, and $B_2 = 3.8 \times 10^{-7}$ for the faster process. These overall three independent relaxation pathways are in agreement with the temperature-dependent data at a fixed DC external field where also three independent processes were observed in the Cole–Cole plots.

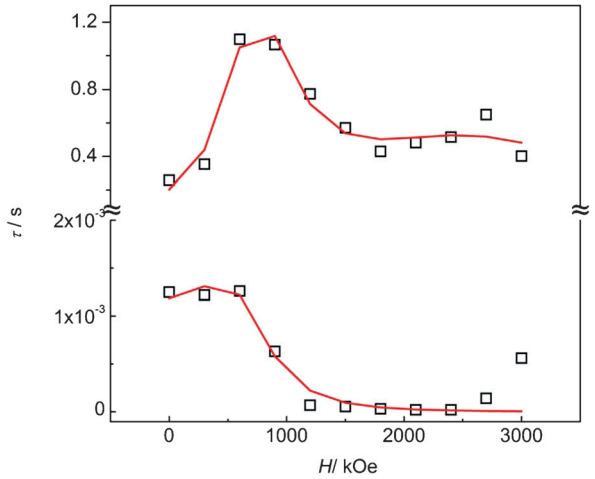

Figure 8. Field dependence of the characteristic relaxation time at 2 K for compound **2**. Squares = experimental data, lines = best fitting curves (see main text).

In the case of complex **1** the χ'' versus T data plots at different frequencies show a similar profile for the three different explored static external DC fields (Figure 9). An incipient not clearly resolved second relaxation process can be distinguished at low temperatures. From Cole–Cole data plots it was possible to assign a second relaxation time for the data achieved under applied DC fields of 1500 and 2200 Oe. Employing Equation (7) allows the extraction of the dynamic relaxation best fitting parameters at the three explored DC fields with more than one possible set in some cases. At 500 Oe these are $U_{eff} = 129$ K, $\tau_0 = 1.0 \times 10^{-10}$ s, $C_{Ram} = 3.5 \times 10^{-2}$ s^{-1} K^{-5} and $\tau_{QT} = 0.27$ s ($n = 5$) and at 1500 Oe these are $U_{eff} = 56$ K, $\tau_0 = 2.3 \times 10^{-7}$ s, $\tau_{QT} = 5.1 \times 10^{-3}$ s or without Orbach component, $C_{Ram} = 1.7 \times 10^{-3}$ s^{-1} K^{-7} and $\tau_{QT} = 5.6 \times 10^{-3}$ s ($n = 7$; fast process) as well as $U_{eff} = 58$ K, $\tau_0 = 1.7 \times 10^{-7}$ s, $\tau_{QT} = 5.5 \times 10^{-2}$ s or with an additional Raman component, two alternative sets, that is, $U_{eff} = 70$ K, $\tau_0 = 3.7 \times 10^{-8}$ s, $C_{Ram} = 1.5 \times 10^{-3}$ s^{-1} K^{-5}, $\tau_{QT} = 7.7 \times 10^{-2}$ s ($n = 5$) or $U_{eff} =$

72 K, $\tau_0 = 3.7\times10^{-8}$ s, $C_{Ram} = 6.9\times10^{-4}$ s^{-1} K^{-7}, $\tau_{QT} = 6.7\times10^{-2}$ s ($n = 7$; slow process); at 2200 Oe these are $U_{eff} = 67$ K, $\tau_0 = 4.1\times10^{-8}$ s, $\tau_{QT} = 1.8\times10^{-2}$ s or with an additional Raman component, $U_{eff} = 80$ K, $\tau_0 = 9.5\times10^{-9}$ s, $C_{Ram} = 1.5\times10^{-2}$ s^{-1} K^{-5}, $\tau_{QT} = 2.0\times10^{-2}$ s ($n = 5$; fast process) and $U_{eff} = 97$ K, $\tau_0 = 1.3\times10^{-9}$ s, $C_{Ram} = 3.4\times10^{-2}$ s^{-1} K^{-5}, $\tau_{QT} = 0.11$ s ($n = 5$; slow process).

The characteristic relaxation times at each different scanned static DC field from the Cole–Cole plots at 2 K were extracted through Equation (8). This allows obtaining the τ versus H profile (Figure 10). In contrast with what was observed in the case of complex **2**, here, three independent pathways with similar characteristic times can be distinguished. They are feasible of fitting with Equation (9), separately for each pathway: $A_1 = 3.2\times10^{-12}$ s^{-1} K^{-1} Oe^{-4} as well as $B_1 = 32$ s^{-1} and $B_2 = 2.1\times10^{-5}$ Oe^{-2} (τ_1) and $B_1 = 5\times10^4$ s^{-1} and $B_2 = 4.0\times10^{-4}$ Oe^{-2} (τ_2, only QT mechanism) and $A_1 = 3.5\times10^{-13}$ s^{-1} K^{-1} Oe^{-4}, $B_1 = 1\times10^4$ s^{-1}, and $B_2 = 2.1\times10^{-3}$ Oe^{-2}.

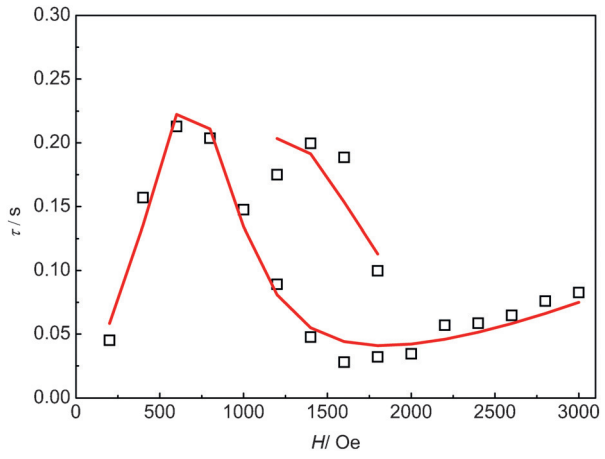

Figure 10. Field dependence of the characteristic relaxation time at 2 K for compound **1**. Squares = experimental data, lines = best fitting curves (see main text).

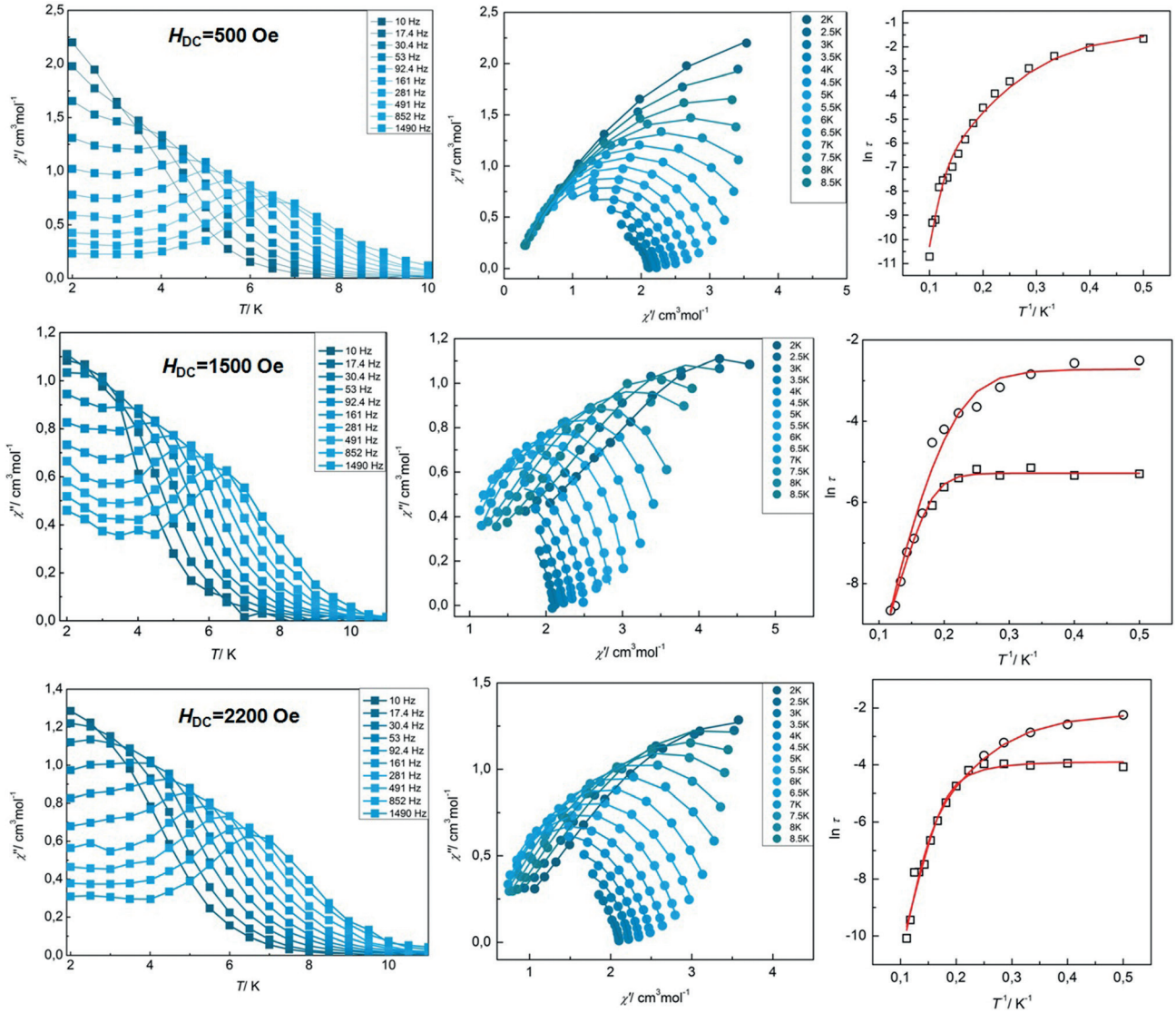

Figure 9. Left: frequency dependence of the out-of-phase AC susceptibility χ_m'' of complex **1** at the specified DC magnetic field in the temperature range 2–10 K. Middle: Cole–Cole plots (circles) with best fitting (see text; lines) in the temperature range 2–8.5 K. Right: $\ln\tau$ versus T^{-1} plots (open symbols) together with best fitting plots (see main text; full line). Circles = slow process (S), squares = fast process (F). Time is given in seconds.

All the dynamic data extracted from the AC susceptibility measurements of complexes **1** and **2** are summarized in Table 1. As frequently observed in lanthanide SMMs, the magnetization relaxation mechanisms are far from being trivial.[18] Moreover, overlapped Orbach and Raman mechanisms make a simple analysis even more difficult. In the case of the herein studied complexes, in spite of bearing a unique Dy^{III} site (imposed crystallographic inversion center or C_2 axis), multi-relaxation steps are evident. When looking at the dynamic data at a zero DC field and some selected small applied external fields, at least two relaxation processes are detected in the case of complex **1** and three in the case of complex **2**. Due to possible Raman contributions, Orbach thermal barriers cannot be definitely established.

Regarding complex **1**, it seems that one thermal barrier close to 60 K and another one close to 100 K could be operative, suggesting relaxation pathways through first and second excited doublet states. From the experimentally extracted crystal-field parameters, these doublet states should be located at 140 and 200 cm^{-1} affording barriers of 200 and 290 K. Multiple quantum tunneling pathways are also observed suggesting that in addition to the ground doublet QTM, thermal-assisted tunneling (TA-QTM) it is also possible. A complex field-dependence pattern is found for these temperature-independent re-

Table 1. Magnetization relaxation dynamic parameters extracted from the experimental data.

H [Oe]	**1**		**2**		
0	$U_{eff}=78$ K $\tau_0=2.9\times10^{-8}$ s $C_R=3.6\times10^{-2}$ $s^{-1}K^{-5}$ $\tau_{QT}=1.8\times10^{-2}$ s ----- $U_{eff}=115$ K $\tau_0=1.2\times10^{-9}$ s $C_R=1.3\times10^{-3}$ $s^{-1}K^{-7}$ $\tau_{QT}=2.6\times10^{-2}$ s		$U_{eff}=51$ K[a] $\tau_0=6.1\times10^{-7}$ s $\tau_{QT}=7.3$ s	$U_{eff}=127$ K[a] $\tau_0=1.2\times10^{-9}$ s $C_R=1.7\times10^{-3}$ $s^{-1}K^{-5}$	
500	$U_{eff}=129$ K $\tau_0=1.0\times10^{-10}$ s $C_R=3.5\times10^{-2}$ $s^{-1}K^{-5}$ $\tau_{QT}=0.27$ s				
1000			$U_{eff}=59$ K $\tau_0=1.7\times10^{-7}$ s $\tau_{QT}=0.58$ s	$U_{eff}=89$ K $\tau_0=5.4\times10^{-8}$ s $C_R=5.5\times10^{-3}$ $s^{-1}K^{-5}$ ----- $U_{eff}=104$ K $\tau_0=2.2\times10^{-8}$ s $C_R=1.7\times10^{-4}$ $s^{-1}K^{-7}$ ----- $C_R=2.2\times10^{-4}$ $s^{-1}K^{-7}$	$\tau_{QT}=2.0\times10^{-4}$ s
1500	$U_{eff}=56$ K $\tau_0=2.3\times10^{-7}$ s $\tau_{QT}=5.1\times10^{-3}$ s ----- $C_R=1.7\times10^{-3}$ $s^{-1}K^{-7}$ $\tau_{QT}=5.6\times10^{-3}$ s	$U_{eff}=58$ K $\tau_0=1.7\times10^{-7}$ s $\tau_{QT}=5.5\times10^{-2}$ s ----- $U_{eff}=70$ K $\tau_0=3.7\times10^{-8}$ s $C_R=1.5\times10^{-3}$ $s^{-1}K^{-5}$ $\tau_{QT}=7.7\times10^{-2}$ s ----- $U_{eff}=72$ K $\tau_0=3.7\times10^{-8}$ s $C_R=6.9\times10^{-4}$ $s^{-1}K^{-7}$ $\tau_{QT}=6.7\times10^{-2}$ s			
2200	$U_{eff}=67$ K $\tau_0=4.1\times10^{-8}$ s $\tau_{QT}=1.8\times10^{-2}$ s ----- $U_{eff}=80$ K $\tau_0=9.5\times10^{-9}$ s $C_R=1.5\times10^{-2}$ $s^{-1}K^{-5}$ $\tau_{QT}=2.0\times10^{-2}$ s	$U_{eff}=97$ K $\tau_0=1.3\times10^{-9}$ s $C_R=3.4\times10^{-2}$ $s^{-1}K^{-5}$ $\tau_{QT}=0.11$ s			

[a] From reference [10].

laxation mechanisms. A possible explanation of this complexity relies on several level crossings due to the very small exchange interaction between the Dy^{III} sites.

A very similar picture is found for complex **2**, with two thermal-activated Orbach processes with barriers close to 60 and 100 K, which in this case agree much better with the crystal-field data that afford first two excited doublet states at 40 and 100 cm^{-1}, equivalent to approximately 30 and 70 K. This better agreement can be possibly understood in terms of a small contribution of transversal crystal-field components, which allows a more reliable DC magnetic data fitting. Here, again multiple quantum tunneling mechanisms are distinguished with a non-trivial field-dependence behavior.

Conclusions

We have successfully tuned the local environment of Dy^{III} in a butterfly-type $\{Co^{III}_2Dy^{III}_2\}$ complex in a remote way by incorporation of close-shell Co^{III} ions to the structure, affording a final $\{Co^{III}_4Dy^{III}_2\}$ moiety. The dominant axial crystal-field components of complexes **1** and **2** allowed obtaining DC susceptibility and magnetization data of pseudo-single-crystal type after crystallite alignment under external magnetic fields.

From the experimentally obtained crystal-field parameters, through employment of a rough electrostatic model, an estimation of the orientation of the main quantization axis can be extracted. This axis is not coincident with the a-priori geometrically established SAP geometry but with a BTP one. It is evident that differences in the charge density over coordinating O atoms together with short versus long Dy^{III}–O bond lengths must be seriously considered in order to rationalize the orientation of the molecular magnetic moment.

Dynamic studies of the magnetization relaxation show a complex multiple relaxation pathway scheme, involving more than one excited state for the thermal-activated Orbach process, with a possible overlapping Raman mechanism. In addition, QTM and thermal-assisted QTM pathways are clearly detected. The estimated energy barriers roughly agree with the DC magnetic data energy level splitting.

Further research is needed to provide a deeper understanding of the magnetization relaxation behavior in this $\{Co^{III}_2Dy^{III}_2\}$ family. A more exhaustive field, frequency, and temperature dependence of the AC data, as well as independent local probe techniques measurements like EPR or FIR spectroscopy would be valuable tools.

Experimental Section

Material and physical measurements

$[Co_2(\mu\text{-}OH_2)(\mu\text{-}piv)_2(piv)_2(Hpiv)_4]$ (piv = trimethylacetate) was prepared following a previously reported procedure.[19] $Dy(NO_3)_3{\cdot}xH_2O$ was prepared by reaction of Dy_2O_3 with nitric acid in water. All other chemicals were of reagent grade and used as receive without further purification. Elemental analysis for C, H, and N were performed with a Carlo Erba 1108 analyzer.

Synthesis of $[Co^{III}_4Dy^{III}_2(OH)_2(teaH)_2(tea)_2(Piv)_6]{\cdot}(CH_3)_3CCOOH{\cdot}2\,CH_3OH$ (1)

$[Co_2(\mu\text{-}OH_2)(\mu\text{-}piv)_2(piv)_2(Hpiv)_4]$ (100 mg, 0.1 mmol) and $Dy(NO_3)_3{\cdot}xH_2O$ (68 mg, ≈0.1 mmol) were dissolved in methanol (10 mL), followed by the addition of triethanolamine (60 mg, 0.4 mmol) and triethylamine (61 mg, 0.6 mmol) dissolved in methanol (10 mL) affording a purple solution. The latter was then stirred at room temperature for one hour, filtered, and allowed to stand sealed. After four weeks the seal was removed and the solution was left for slowly evaporation. Within three to four weeks a crop of blue plates crystallized in an approximate yield of 22% (30.9 mg). Elemental analysis calcd (%) for $C_{61}H_{124}Co_4Dy_2N_4O_{30}$: C 37.5, H 6.5, N 2.9; found: C 37.3, H 6.4, N 2.8.

Magnetic measurements

Magnetic measurements were performed with a Quantum Design MPMS XL-7 SQUID magnetometer. All experimental magnetic data were corrected for the diamagnetism of the sample holders and the constituent atoms (Pascal tables). DC measurements were conducted from 2 to 300 K at 1 kOe and between 2 and 10 K in the range of 1–70 kOe. AC measurements were performed at driving frequencies ranging from 10 to 1500 Hz with an AC field amplitude of 3 Oe under a zero DC field and applied fields up to 2200 Oe. In the samples where free movement of crystallites was prevented, silicone grease was employed for the embedding. When silicone is not used, the sample completely aligned with field quantization axis as evidenced by the magnetization saturation values achieved.

X-ray structure determination

The crystal structure of compound **1** was determined with an Oxford Xcalibur, Eos, Gemini CCD area-detector diffractometer by using graphite-monochromated $Mo_{K\alpha}$ radiation ($\lambda = 0.71069$ Å) at 298 K. Data was corrected for absorption with CrysAlisPro, Oxford Diffraction Ltd., Version 1.171.33.66, applying an empirical absorption correction by using spherical harmonics, implemented in the SCALE3 ABSPACK scaling algorithm.[20] The structure was solved by direct methods with SIR97[21] and refined by full-matrix least-squares on F^2 with SHELXL-2014[22] under the WinGX platform.[23] Hydrogen atoms were added geometrically and refined as riding atoms with a uniform value of U_{iso}. Hydrogen atoms of bridging hydroxide and pivalic acid solvent molecules both bond to oxygen atoms, were found in the Fourier difference map and further refined with restrained U_{iso} ($1.2\,U_{iso}$(O)). One of the coordinated pivalate methyl groups and the pivalic acid solvent molecule methyl group was found disordered around two positions and was refined as two split positions with 0.5:0.5 occupancy factors. The final crystallographic data and values of R_1 and wR are listed in Table 2. CCDC 1462510 contains the supplementary crystallographic data for this paper. These data can be obtained free of charge from The Cambridge Crystallographic Data Centre via www.ccdc.cam.ac.uk/data_request/cif.

Acknowledgements

We gratefully acknowledge UBA, ANPCYT, and CONICET for funding resources. P.A. is a staff member of CONICET and A.V.F. is a doctoral fellow of CONICET.

Table 2. Crystallographic data of complex **1**.

empirical formula	$C_{61}H_{124}Co_4Dy_2N_4O_{30}$
formula weight [g mol^{-1}]	1954.61
T [K]	298(2)
crystal system	monoclinic
space group	$C2/c$
a [Å]	29.510(4)
b [Å]	12.510(6)
c [Å]	26.657(6)
α [°]	90
β [°]	110.54(2)
γ [°]	90
V [Å^3]	9215.35
Z	4
D_{calcd} [mg m^{-3}]	1.528
absorption coefficient [mm^{-1}]	2.383
F(000)	4360
λ [Å]	0.71069
θ range data collection [°]	3.56–29.05
index ranges	$-30 \le h \le 37$
	$-15 \le k \le 15$
	$-33 \le l \le 33$
reflns. collected/unique	19666/9839
Rint	0.0850
observed reflns. [$I > 2\sigma(I)$]	6601
completeness [%]	97.8
max./min. transmission	1.0000/0.589
data/restraints/parameters	9839/9/518
GOF on F^2	1.060
final R index [$I > 2\sigma(I)$]/ all data	0.0619/0.0981
wR index [$I > 2\sigma(I)$]/all data	0.1307/0.1652
largest peak and hole [e A^{-3}]	−1.435 and 1.744
weights, w	$1/[\sigma^2(F_o^2)+(0.0472P)^2+28.1253P]$ where $P=(F_o^2+2F_c^2)/3$

Keywords: dysprosium · coordination complex · lanthanides · magnetic properties · single-molecule magnets

[1] a) D. N. Woodruff, R. E. P. Winpenny, R. A. Layfield, *Chem. Rev.* **2013**, *113*, 5110; b) L. Sorace, C. Benelli, D. Gatteschi, *Chem. Soc. Rev.* **2011**, *40*, 3092; c) J. D. Rinehart, J. R. Long, *Chem. Sci.* **2011**, *2*, 2078; d) R. Sessoli, A. K. Powell, *Coord. Chem. Rev.* **2009**, *253*, 2328.

[2] D. Gatteschi, R. Sessoli, J. Villain, *Molecular Nanomagnets*, Oxford University Press, Oxford, **2006**.

[3] a) M. Affronte, F. Troiani, in *Molecular Magnets: Physical Applications* (Eds.: J. Bartolome, J. Luis, F. Fernandez), Springer, Heidelberg, **2014**, pp. 249–273; b) M. Mannini, F. Pineider, P. Sainctavit, C. Danieli, E. Otero, C. Sciancalepore, A. M. Talarico, M. A. Arrio, A. Cornia, D. Gatteschi, R. Sessoli, *Nat. Mater.* **2009**, *8*, 194; c) M. Affronte, *J. Mater. Chem.* **2009**, *19*, 1731; d) F. Troiani, M. Affronte, *Chem. Soc. Rev.* **2011**, *40*, 3119; e) M. N. Leuenberger, D. Loss, *Nature* **2001**, *410*, 789.

[4] a) S. Sanvito, *Chem. Soc. Rev.* **2011**, *40*, 3336; b) L. Bogani, W. Wersndorfer, *Nat. Mater.* **2008**, *7*, 179.

[5] a) N. Ishikawa, M. Sugita, T. Ishikawa, S. Koshihara, Y. Kaizu, *J. Phys. Chem. B* **2004**, *108*, 11265; b) N. Ishikawa, M. Sugita, T. Ishikawa, S. Koshihara, Y. Kaizu, *J. Am. Chem. Soc.* **2003**, *125*, 8694.

[6] S. T. Liddle, J. van Slageren, *Chem. Soc. Rev.* **2015**, *44*, 6655.

[7] a) F. Habib, M. Murugesu, *Chem. Soc. Rev.* **2013**, *42*, 3278; b) P. Zhang, Y.-N. Guo, J. K. Tang, *Coord. Chem. Rev.* **2013**, *257*, 1728.

[8] a) K. Liu, W. Shi, P. Cheng, *Coord. Chem. Rev.* **2015**, *289–290*, 74; b) L. Rosado Piquer, E. C. Sañudo, *Dalton Trans.* **2015**, *44*, 8771; c) H. L. C. Feltham, S. Brooker, *Coord. Chem. Rev.* **2014**, *276*, 1.

[9] a) S. K. Langley, C. Le, L. Ungur, B. Moubaraki, B. F. Abrahams, L. F. Chibotaru, K. S. Murray, *Inorg. Chem.* **2015**, *54*, 3631; b) S. K. Langley, N. F. Chilton, B. Moubaraki, K. S. Murray, *Inorg. Chem. Front.* **2015**, *2*, 867; c) S. K. Langley, L. Ungur, N. F. Chilton, B. Moubaraki, L. F. Chibotaru, K. S. Murray, *Inorg. Chem.* **2014**, *53*, 4303; d) S. K. Langley, N. F. Chilton, B. Moubaraki, K. S. Murray, *Inorg. Chem.* **2013**, *52*, 7183; e) S. K. Langley, N. F. Chilton, B. Moubaraki, K. S. Murray, *Chem. Commun.* **2013**, *49*, 6965; f) S. K. Langley, N. F. Chilton, L. Ungur, B. Moubaraki, L. F. Chibotaru, K. S. Murray, *Inorg. Chem.* **2012**, *51*, 11873.

[10] A. V. Funes, L. Carrella, E. Rentschler, P. Alborés, *Dalton Trans.* **2014**, *43*, 2361.

[11] a) A. V. Funes, L. Carrella, L. Sorace, E. Rentschler, P. Alborés, *Dalton Trans.* **2015**, *44*, 2390; b) I. C. Lazzarini, A. V. Funes, L. Carrella, L. Sorace, E. Rentschler, P. Alborés, *Eur. J. Inorg. Chem.* **2014**, 2561; c) I. C. Lazzarini, L. Carrella, E. Rentschler, P. Alborés, *Polyhedron* **2012**, *31*, 779; d) P. Alborés, E. Rentschler, *Angew. Chem. Int. Ed.* **2009**, *48*, 9366; *Angew. Chem.* **2009**, *121*, 9530; e) P. Alborés, E. Rentschler, *Dalton Trans.* **2009**, 2609.

[12] S. Alvarez, P. Alemany, D. Casanova, J. Cirera, M. Llunell, D. Avnir, *Coord. Chem. Rev.* **2005**, *249*, 1693.

[13] N. F. Chilton, R. P. Anderson, L. D. Turner, A. Soncini, K. S. Murray, *J. Comput. Chem.* **2013**, *34*, 1164.

[14] a) J. Long, F. Habib, P.-H. H. Lin, I. Korobkov, G. Enright, L. Ungur, W. Wersndorfer, L. F. Chibotaru, M. Murugesu, *J. Am. Chem. Soc.* **2011**, *133*, 5319; b) E. Moreno Pineda, N. F. Chilton, R. Marx, M. Dörfel, D. O. Sells, P. Neugebauer, S.-D. Jiang, D. Collison, J. van Slageren, E. J. L. McInnes, R. E. P. Winpenny, *Nat. Commun.* **2014**, *5*, 5243.

[15] N. F. Chilton, D. Collison, E. J. L. McInnes, R. E. P. Winpenny, A. Soncini, *Nat. Commun.* **2013**, *4*, 2551.

[16] a) J. J. Baldoví, J. M. Clemente-Juan, E. Coronado, A. Gaita-Ariño, A. Palii, *J. Comput. Chem.* **2014**, *35*, 1930; b) J. J. Baldoví, J. M. Clemente-Juan, E. Coronado, A. Gaita-Ariño, *Inorg. Chem.* **2014**, *53*, 11323.

[17] A. Abraham, B. Bleaney, *Electron Paramagnetic Resonance of Transition Ions*, Oxford University Press, Oxford, **1970**.

[18] See, for example: a) M. Gregson, N. F. Chilton, A.-M. Ariciu, F. Tuna, I. F. Crowe, W. Lewis, A. J. Blake, D. Collison, E. J. L. McInnes, R. E. P. Winpenny, S. T. Liddle, *Chem. Sci.* **2016**, *7*, 155; b) M. R. Silva, P. Martín-Ramos, J. T. Coutinho, L. C. J. Pereira, V. Lavín, I. R. Martín, P. S. P. Silva, J. Martín-Gil, *Dalton Trans.* **2015**, *44*, 1264; c) P. Martín-Ramos, M. Ramos Silva, J. T. Coutinho, L. C. J. Pereira, P. Chamorro-Posada, J. Martín-Gil, *Eur. J. Inorg. Chem.* **2014**, 511; d) E. Lucaccini, L. Sorace, M. Perfetti, J.-P. Costes, R. Sessoli, *Chem. Commun.* **2014**, *50*, 1648; e) S. Xue, L. Ungur, Y. Guo, J. K. Tang, L. F. Chibotaru, *Inorg. Chem.* **2014**, *53*, 12658; f) Y.-N. Guo, G.-F. Xu, Y. Guo, J. K. Tang, *Dalton Trans.* **2011**, *40*, 9953; g) M. Jeletic, P. Lin, J. J. Le Roy, I. Korobkov, S. I. Gorelsky, M. Murugesu, *J. Am. Chem. Soc.* **2011**, *133*, 19286; h) S. D. J. S. D. Jiang, B. W. Wang, H. L. Sun, Z. M. Wang, S. Gao, *J. Am. Chem. Soc.* **2011**, *133*, 4730; i) A. Watanabe, A. Yamashita, M. Nakano, T. Yamamura, T. Kajiwara, *Chem. Eur. J.* **2011**, *17*, 7428.

[19] G. Aromí, A. S. Batsanov, P. Christian, M. Helliwell, A. Parkin, S. Parsons, A. A. Smith, G. A. Timco, R. E. P. Winpenny, *Chem. Eur. J.* **2003**, *9*, 5142.

[20] SCALE3 ABSPACK, Empirical absorption correction, CrysAlis-Software package, Oxford Diffraction Ltd., Oxford, **2006**.

[21] A. Altomare, M. C. Burla, M. Camalli, G. L. Cascarano, C. Giacovazzo, A. Guagliardi, A. G. G. Moliterni, G. Polidori, R. Spagna, *J. Appl. Crystallogr.* **1999**, *32*, 115.

[22] G. M. Sheldrick, *Acta Crystallogr. Sect. A* **2008**, *64*, 112.

[23] L. J. Farrugia, *J. Appl. Crystallogr.* **2012**, *45*, 849.

Received: June 6, 2016
Published online on August 16, 2016